IV International Conference on Simulation for Additive Manufacturing
Sim-AM 2023
E. Rank and S. Kollmannsberger (Eds)

CELLULAR AUTOMATA SIMULATION OF FULLY EQUIAXED MICROSTRUCTURE FORMATION IN SCALMALLOY DURING ADDITIVE MANUFACTURING WITH ADJUSTABLE RING MODE LASER

MOHAMMAD S. MOHEBBI[*] AND VASILY PLOSHIKHIN

[*] Airbus Endowed Chair for Integrative Simulation and Engineering of Materials and Processes (ISEMP), University of Bremen
Am Fallturm 1, 28359, Bremen, Germany
e-mail: mohebbi@isemp.de, https://www.bccms.uni-bremen.de/isemp/

Keywords: Numerical simulation, Cellular automata, Powder-bed fusion, Ring-mode laser, Sc-Zr-modified aluminum alloys

Abstract. We utilized an Adjustable Ring-Mode (ARM) laser to achieve an almost fully equiaxed microstructure in powder bed Fusion-laser beam Scalmalloy®. ARM laser-built specimens exhibited over 90% fine-grained material, while circular laser-built specimens yielded less than 50% fine-grained material, using the same laser power, speed, and hatch spacing. To gain insights into these interesting results, we employed a Cellular Automata (CA) solidification simulation, incorporating the nucleation role of L12 $Al_3(Sc_xZr_{1-x})$ precipitates through a particle-based nucleation model. The simulation was coupled with the corresponding temperature field derived from finite difference analyses of the circular and ARM laser beams. The simulation results revealed a significantly thicker precipitation zone (equiaxed grains) under the ARM laser compared to the circular beam, primarily attributed to reduced temperature and cooling rates. The excellent correlation between simulation and experimental results demonstrates promising potential for the predictive application of the developed model. It can be effectively utilized to optimize heat source modulation and process parameters, thereby enabling the adaptation of microstructure and mechanical properties.

1 INTRODUCTION

The increasing need for lightweight and durable structural alloys suitable for Additive Manufacturing (AM) processes, particularly Powder Bed Fusion - Laser Beam (PBF-LB), has led to the development of innovative Sc- and Zr-modified Al alloys. One widely used commercially available alloy, known as Scalmalloy®, has a nominal composition (wt%) of Al-4.6Mg-0.66Sc-0.42Zr-0.49Mn [1,2]. The remarkable influence of Sc and Zr elements is primarily attributed to their nanoscale precipitates, such as the L12 $Al_3(Sc_xZr_{1-x})$ phase, which plays crucial roles in grain refinement, grain boundary stability, and temperature resistance. In

these alloys, the as-built grain structure consists of two distinct regions: an equiaxed ultrafine-grained (FG) band at the boundary of the melt pool and a relatively columnar and coarse-grained (CG) region at the core of the melt pool [3]. However, depending on the process conditions, the CG region still accounts for 50-80% of the microstructure. Consequently, since the introduction of these alloys, there has been considerable interest in further refining the microstructure by increasing the fraction of the FG region and ideally achieving a fully equiaxed microstructure [4].

The formation of ultrafine equiaxed grains in the FG band can be attributed to the L12 particles, which act as ideal nuclei due to their excellent lattice match with α-Al. Therefore, efforts to expand the FG band primarily involve stimulating such nucleation (fusion-boundary nucleation) through the application of an appropriate temperature field [4–6]. Modeling and simulating the development of such a bimodal microstructure in PBF-LB Al alloys are essential for understanding, predicting, and optimizing the process outcomes. In our previous works, we developed a Cellular-Automata (CA) approach that incorporates physics-based nucleation features in Al alloys, such as AlSi10Mg [7] and Scalmalloy® [17]. The fusion boundary nucleation in Sc-Zr-modified Al alloys was modeled by the evolution of L12 particles during melting and solidification. This approach successfully predicted the distinct FG and CG regions within the laser track, as well as the experimentally observed enhanced FG band, achieved through platform heating and reduced scanning speed [17].

In addition to the standard parameters, heat source modulation has the potential to control the thermal field of the melt pool and the associated solidification conditions. For instance, Shi et al. [8] revealed that a transverse elliptical beam shape promotes nucleation events and equiaxed grains in stainless steel 316L. The Adjustable Ring-Mode (ARM) laser, which combines a ring-mode laser beam with a centered conventional Gaussian (circular) laser beam, is a popular example in welding applications, particularly as a promising method for joining difficult-to-weld metal components like some Al alloys [9,10]. The ability of the ARM laser to modulate the applied temperature field holds promise for regulating AM solidification microstructures. However, the application of this laser mode in AM is relatively rare in the literature [11,12].

Considering the potential of an ARM laser to modify the temperature field of the melt pool and the aforementioned demand for grain refinement in Sc-Zr-modified Al alloys, the present study aims to investigate the influence of an ARM laser beam on the solidification microstructure of Scalmalloy®, providing a better understanding of the microstructural refinement using cellular automata solidification simulation powered by the particle-based nucleation.

2 EXPERIMENTS

Cubic specimens with a contour of 10×10 mm² and a height of 15 mm were produced using pre-alloyed Scalmalloy® powder on an AconityMIDI machine equipped with a programmable nLIGHT AFX-1000 fiber laser. The process parameters used were as follows: a laser power of 370 W, a scanning speed of 1000 mm/s, a hatch distance of 100 µm, and a layer thickness of 30 µm, resulting in a volumetric energy density of 123 J/mm³. The platform was preheated to 200 °C. Two sets of specimens were manufactured using circular and ARM laser beams (Fig. 1). The circular beam had a nominal spot diameter of 130 µm, with a

measured diameter at 1/e³ of 116 µm. The ARM laser beam with the nominal dimensions shown in Fig. 1b had an 89% power ratio in the ring and 11% in the center. The measured diameters at 1/e³ were 358 µm (outer), 154 µm (inner), and 146 µm (center). A bi-directional scanning strategy was employed, with an alternating layer-wise rotation of +90 and -90°.

The melt pool dimensions and the thickness of the FG band were characterized using optical microscopy near the top surface and the center of the vertical cross-sections. Additionally, the grain structures were analyzed using Electron Backscatter Diffraction (EBSD) in regions near the center of the vertical cross-sections. An area of 250×250 µm² was scanned with a step size of 0.5 µm.

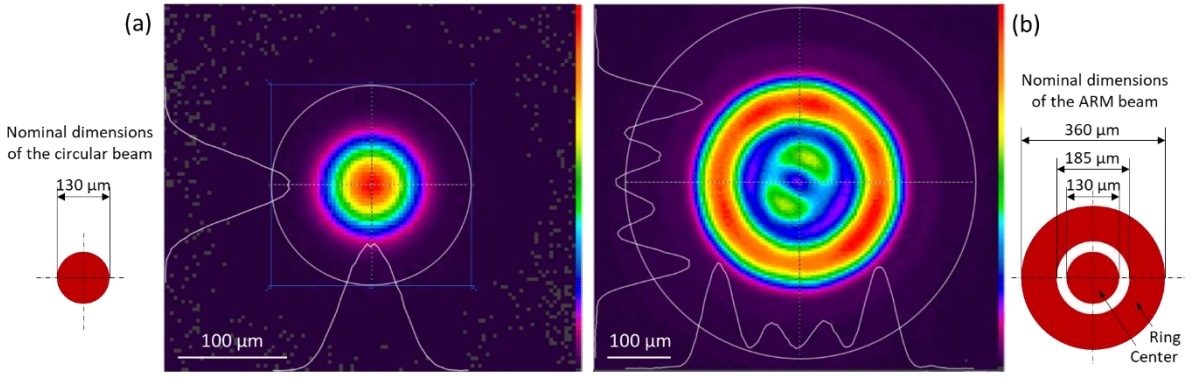

Figure 1: Beam nominal dimensions and measured intensity distribution in (a) circular, and (b) ARM laser beams (measurements provided by Aconity3D).

3 PRECIPITATION MODEL

In this section, we describe the precipitation modeling approach used in our study to estimate the precipitate number density as potential nucleation sites for α-Al. The model is integrated into the CA solidification simulation to simulate the grain structure evolution during PBF-LB with circular and ARM beams.

The primary L12 precipitation is treated with an initiation criterion (particle nucleation) and an evolution model of particle fraction and number density. The particle nucleation incubation time (τ_0) can be expressed as [13]:

$$\tau_0 = \frac{7.2 R_g f(\theta)}{1-\cos\theta} \cdot \frac{a^4}{d_a^2 x_{\text{eff}}} \cdot \frac{T_r}{D_u \Delta S_m \Delta T_r^2} \tag{1}$$

where R_g is the gas constant, θ is the wetting angle reported as 90° [14], $f(\theta) = 0.25(2+\cos\theta)(1-\cos\theta)^2$, a is the atomic jump distance, d_a is the average diameter of the particle phase, x_{eff} is the effective alloy concentration that equals the ratio of the mole fraction of Sc in liquid to that of the particle, $T_r = T/T_{l,p}$, $T_{l,p}$ is the liquidus temperature of the precipitating phase, $\Delta T_r = 1 - T_r$, D_u is diffusivity in the undercooled melt, and ΔS_m is the molar entropy of fusion. D_u is estimated from the Stokes-Einstein equation [15]:

$$D_u = \frac{k_B T}{6\, d_{a,l}\, 10^{-3.3} \exp\left(3.34 T_{l,p}/(T - T_{l,p}/3)\right)} \tag{2}$$

in which k_B is Boltzmann's constant and $d_{a,l}$ is the average distance between liquid atoms ($\cong d_a$).

Once the initiation criterion is met, the progress of precipitation is treated by the so-called Avrami equation. The approach proposed by Vazquez et al. [16] is employed to generalize the model to non-isothermal ($T(t_r)$) phase transformation and evolution of the fraction of particles (f_p) versus the relative time ($t_r = t - \tau_0$):

$$\frac{df_p}{dt_r} = nk_a\left(f_\infty - f_p\right) I^{n-1} \qquad I = \int_0^{t_r} k_a\left(T(t')\right)dt' \tag{3}$$

where k_a is the rate constant, n is the Avrami exponent and f_∞ is the thermodynamically achievable fraction of particles. Eq. 3 determines the variation of particle fraction at a given time. Therefore, the integrated amount of particle fraction at each point of the material is a function of the temperature history. Along with the evolution of $f_{r,p}$, the development of the particle number density (N_p) can be calculated based on the rate of particle nucleation being inversely proportional to the incubation time τ_0. Table 1 provides the parameters used in the model.

Table 1: Parameters used in the primary L12 precipitation model and FD analyses

Model parameters	Value	Heat source parameters	Value
θ (°)	90	Circular beam:	
a (m)	5×10^{-10}	Laser absorption	0.44
d_a (m)	2.54×10^{-10}	Radius (μm)	90
x_{eff}	0.016	Depth (μm)	7
$T_{l,p}$ (K)	1000		
ΔS_m (J/mol.K)	12.8	ARM beam:	
k_a	5×10^{-7}	Laser absorption	0.65
n	2	Center radius (μm)	73
f_∞	0.017	Ring outer radius (μm)	179
C_n	10^{20}	Ring inner radius (μm)	77
P_{np}	0.03	Depth (μm)	12

4 GRAIN STRUCTURE SIMULATION

The precipitation kinetic model was incorporated into the CA simulation of the grain structure evolution during solidification. Firstly, the thermal field was calculated using a Finite Difference (FD) approach. Detailed information on the thermal simulation methodology and material properties can be found in our previous papers [17,18], where the circular beam was modeled by a standard Gaussian heat distribution:

$$q = \frac{6\sqrt{3}\,p_c}{\pi\sqrt{\pi}r^2c}\exp\left(-3\left(\frac{x^2+y^2}{r^2}+\frac{z^2}{c^2}\right)\right) \tag{4}$$

in which q represents the local heat flux, *x*,*y*, and *z* are the local coordinates with respect to the heat source, p_c is the absorbed circular beam power, and r and c are the effective radius and depth of the heat source, respectively. The circular component of the ARM beam is modeled using the same equation. Likewise, the ring component is modeled as:

$$q = \frac{3\,p_r}{\pi^2 r_r \sigma c_r} \exp\left(-3\left(\frac{\left(\sqrt{x^2+y^2}-r_r\right)^2}{\sigma^2}+\frac{z^2}{{c_r}^2}\right)\right) \tag{5}$$

where subscript *r* denotes the parameters of the ring component of the ARM beam, r_r is the average of inner and outer radius and σ is half of their difference.

The calculated temperature field of the moving heat source is then incorporated into the CA analysis to update the common cell attributes for solidification simulation, such as grain index, nucleation index, crystallographic orientation, and state. The primary precipitation model is implicitly integrated into the CA approach by assigning particle-related attributes to the CA cells, such as particle incubation time, particle fraction, and number density, as proposed in our previous work [17]. The particle nucleation criterion is accounted for by modifying the normalized particle formation time of a given cell *v*, τ_v, at temperature T_v, by $\delta t/\tau_0(T_v)$, where δt is the time step. Particles start to develop in a cell when $\tau_v \geq 1$. The CA domain is initialized with a τ_v of unity, which resets to 0 when cells experience a temperature above the particle dissolution temperature. Precipitation in cells with $\tau_v \geq 1$ follows the Avrami model with a CA version of Eq. 3, which is a numerical calculation based on the CA time step. The developed particle number density is directly related to the particle nucleation rate, which is considered to be inversely proportional to the nucleation incubation time:

$$\delta N_{p,v} = \frac{C_n}{\tau_0}\delta f_{p,v} \tag{6}$$

where C_n is the proportionality constant. The probability of a cell for heterogeneous nucleation of α-Al is proportional to its particle number density, $P_{np}N_{p,v}$ where P_{np} is the probability of a particle to accommodate α-Al nucleation.

We employed the developed simulation approach in different scales: a single-hatch 3D model with a cell size of 1 µm, a single-hatch semi-2D model with a cell size of 0.25 µm, and a multi-layer multi-hatch model accommodating 12 layers with 6 hatches in each layer, with a cell size of 1.5 µm. The domains for the single-hatch analyses were 500 µm wide (*y*) and 190 µm deep (*z*), with a length (*x*) of 800 µm for the 3D model and 5 µm for the semi-2D model. The multi-layer domain was 900 × 900 × 460 µm³. For a detailed description of the model formulation, CA solidification, and α-Al nucleation, we refer the readers to our previous papers [7,17]. The parameters used for our simulations in this work are summarized in Table 1.

5 RESULTS AND DISCUSSION

Optical micrographs after etching are presented in Fig. 2, showing the melt pool boundaries from the top-most layer for the calibration of thermal analysis. The width and depth of the melt pools under both circular and ARM beams were measured as the average of about 30 individual melt pool measurements in each specimen. The average melt pool widths

and depths were found to be 84 µm and 209 µm, respectively, for the circular beam, and 95 µm and 352 µm, respectively, for the ARM beam. The relatively wide and shallow melt pools observed in both cases indicate a conduction mode of laser melting [19]. However, the melt pools formed by the ARM laser were notably wider compared to the circular beam, which can be attributed to the broader heat distribution of the ARM laser.

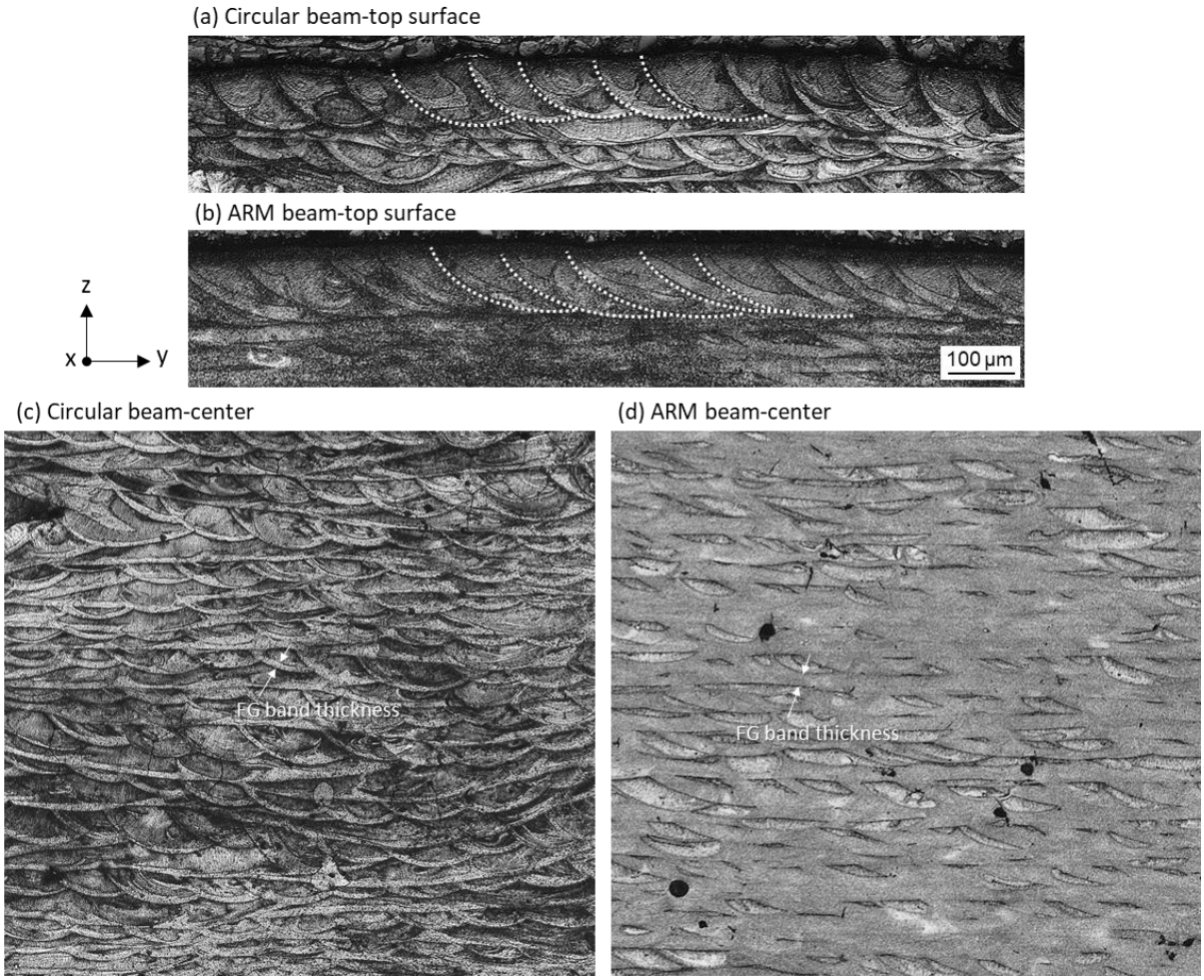

Figure 2: Optical micrographs from the top and center of the circular and ARM laser-built specimens.

Additionally, the thickness of the FG bands was measured across a large area at the center of the *x* cross-sections (Figs. 2c and d). A total of 150 FG bands were measured in each specimen. Consistent with the shape of the melt pools, the ARM beam resulted in a significantly thicker FG band of 23.0 µm, compared to the circular beam, which exhibited an FG band thickness of 9.4 µm. The formation of the FG bands is attributed to the nucleation of α-Al on the L12 precipitates, which form and survive at low cooling rates and temperatures [3,14,20]. Consequently, the thicker FG bands observed with the ARM beam indicate a wider heat distribution and, therefore, lower cooling rates and temperature gradients.

The FD analyses were calibrated using the parameters presented in Table 1, based on the measured melt pool dimensions. Fig. 3 illustrates the resulting thermal fields, showing that the wider heat source of the ARM beam led to a lower maximum temperature and significantly reduced cooling rate and thermal gradient. In the temperature fields, the melting point isotherm is superimposed, indicating a somewhat step-wise penetration by the ARM beam.

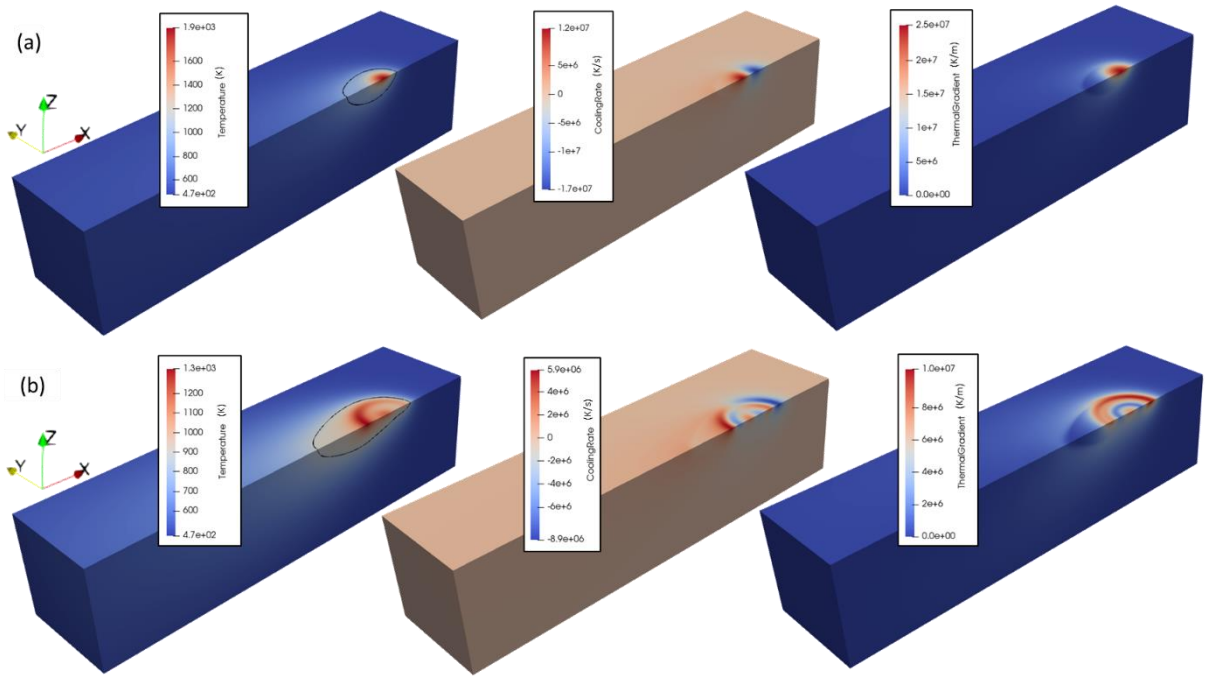

Figure 3: FD thermal fields including temperature, cooling rate and temperature gradient during scanning by (a) circular and (b) ARM laser beams.

Fig. 4 displays the results of the single-track CA analyses using both the 3D and semi-2D approaches. The 3D domain is cut in half to analyze and observe microstructural evolutions in both the y and z planes. The simulation successfully reproduces the bimodal grain structure, with an FG band at the melt pool boundary and a CG region at the center, achieved through the CA simulation coupled with the particle-based nucleation model. The distinct difference between the FG and CG regions can be attributed to two contributing factors in the model.

At the center of the melt pool, temperatures exceed the particle dissolution temperature, indicating that no particles are available during cooling. Therefore, primary precipitation is only expected after the criterion $\tau_v = 1$ is met. This criterion is more difficult to satisfy at the center of the melt pool due to higher cooling rates, resulting in solute trapping rather than primary precipitation. Conversely, at the fusion boundary, the cooling rate is lower, allowing primary particles to precipitate during solidification. Additionally, the temperature remains below the dissolution temperature, meaning that the elapsed incubation time by pre-existing material and previous hatches does not reset to zero. The coupled precipitation model effectively replicates these microstructural features.

Furthermore, the comparison of circular and ARM beam tracks in Fig. 4 confirms the thicker FG band achieved by the ARM beam, consistent with the observations from the experiments (Fig. 2). This aligns with the explained particle-based nucleation model, where the thicker FG band is attributed to the reduced cooling rate and the thickening of the fusion boundary zone below the dissolution temperature. Notably, the obtained FG band thicknesses show good agreement with experimental measurements. The shape of the FG band by the ARM beam exhibits a thinner edge and thicker bottom, closely matching the experimental observations in Fig. 2, which validates the employed thermal field in the simulations.

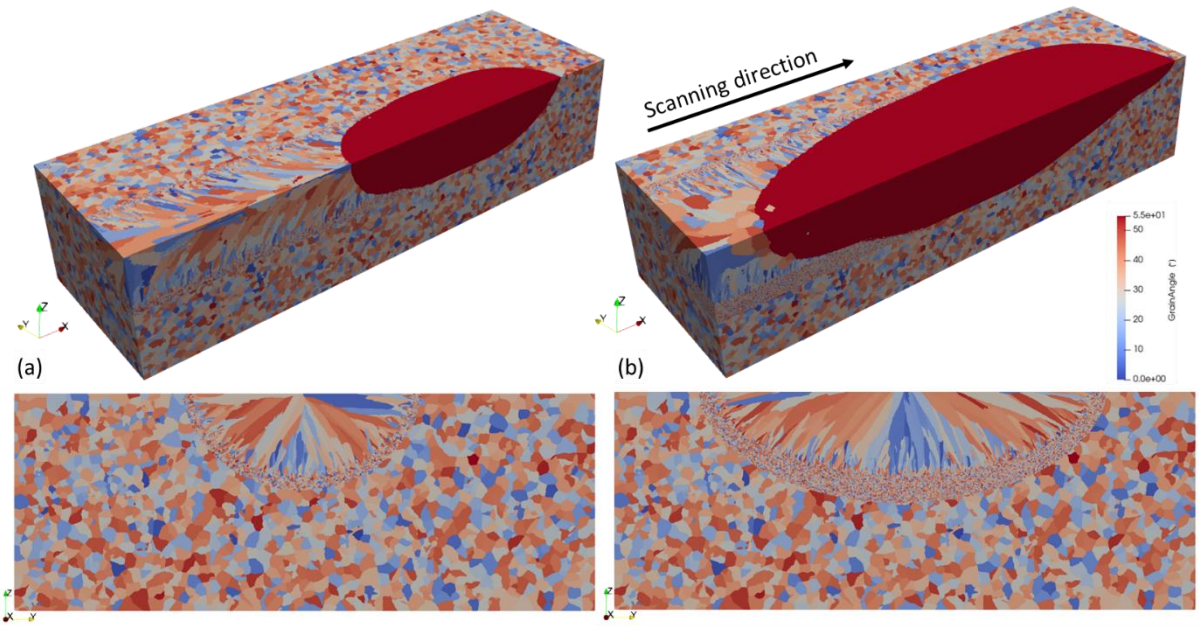

Figure 4: 3D and semi-2D (*x*-section)) CA simulations of single tracks with (a) circular and (b) ARM beams.

Fig. 5 presents micrographs obtained by mesoscale domains with multi-layer multi-hatch simulations. The revealed pattern of the FG bands is a result of the 90° rotation of hatch directions between layers, leading to horizontal bands formed by tracks along the y-axis and curved bands due to the tracks along the x-axis. The corresponding EBSD micrographs are also provided for comparison. Overall, the simulation results show good agreement with the EBSDs, particularly in reflecting the enhanced fraction of the FG region in the ARM laser-built specimen. It is worth noting that the area fraction of the FG region increased from 48% in the circular laser-built specimen to 91% in the ARM laser-built specimen, a result clearly obtained through the CA analyses powered by the particle-based nucleation approach.

It is essential to address the regular pattern of FG and CG regions observed in the simulations, which differs from the relatively irregular distributions in the experiments. This difference can be explained by the perfectly aligned hatches in the simulations, whereas in practical experiments, local fluctuations and hatch deviations are common, resulting in relatively irregular FG and CG regions. Incorporating these deviations into the simulations is expected to yield similar results to the experimental observations.

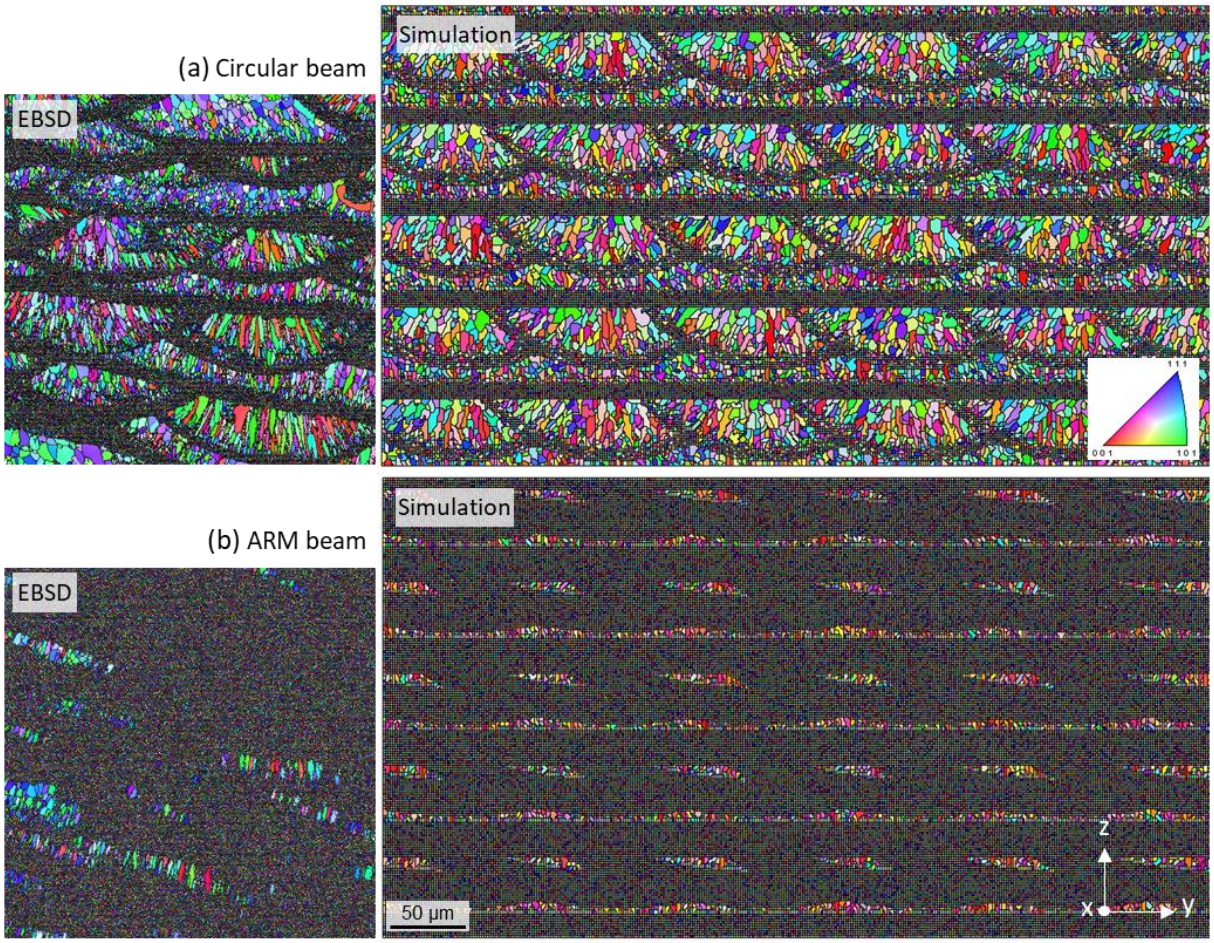

Figure 5: Comparison of experimental (EBSD) and simulation (CA) micrographs obtained from PBF-LB with (a) circular and (b) ARM laser beams.

6 CONCLUSIONS

In conclusion, our study demonstrated the potential of heat source modulation using the ARM laser beam for achieving significant grain refinement in Scalmalloy®, resulting in a nearly fully equiaxed grain structure. We utilized a CA simulation of solidification, powered by a particle-based nucleation model, to gain a comprehensive understanding of this remarkable microstructure refinement. The model considered the evolution of L12 Al3(Sc_xZr_{1-x}) particles, which act as perfect nuclei for α-Aluminum.

The simulation successfully reproduced the bimodal grain structure, with an FG-band at the melt pool boundary and a CG region at the core of the melt pool, through coupling with calibrated thermal analyses. We observed that the enhanced grain refinement by the ARM laser was primarily attributed to the reduced cooling rate, promoting primary precipitation, and expanding the portion of the melt pool below the particle dissolution temperature.

The ability to control microstructure and mechanical properties through heat source modulation presents exciting prospects for future research in additive manufacturing. In this

regard, our presented simulation methodology can accelerate process optimization to achieve these goals.

ACKNOWLEDGMENT

We would like to acknowledge the University of Bremen for their financial support of this contribution. We extend our appreciation to the German Research Foundation (Deutsche Forschungsgemeinschaft) for their financial support through grant number PL 584/4-1. Additionally, we would like to acknowledge Aconity3D GmbH for their valuable contribution by providing us with the essential equipment necessary to conduct our experiments.

REFERENCES

[1] Rometsch PA, Zhu Y, Wu X, Huang A. Review of high-strength aluminium alloys for additive manufacturing by laser powder bed fusion. Mater. Des. 219, 110779 (2022).

[2] Spierings AB, Dawson K, Voegtlin M, Palm F, Uggowitzer PJ. Microstructure and mechanical properties of as-processed scandium-modified aluminium using selective laser melting. CIRP Ann. 65(1), 213–216 (2016).

[3] Spierings AB, Dawson K, Heeling T et al. Microstructural features of Sc- and Zr-modified Al-Mg alloys processed by selective laser melting. Mater. Des. 115, 52–63 (2017).

[4] Yang KV, Shi Y, Palm F, Wu X, Rometsch P. Columnar to equiaxed transition in Al-Mg(-Sc)-Zr alloys produced by selective laser melting. Scr. Mater. 145, 113–117 (2018).

[5] Spierings AB, Dawson K, Uggowitzer PJ, Wegener K. Influence of SLM scan-speed on microstructure, precipitation of Al3Sc particles and mechanical properties in Sc- and Zr-modified Al-Mg alloys. Mater. Des. 140, 134–143 (2018).

[6] Griffiths S, Rossell MD, Croteau J, Vo NQ, Dunand DC, Leinenbach C. Effect of laser rescanning on the grain microstructure of a selective laser melted Al-Mg-Zr alloy. Mater. Charact. 143, 34–42 (2018).

[7] Mohebbi MS, Ploshikhin V. Implementation of nucleation in cellular automaton simulation of microstructural evolution during additive manufacturing of Al alloys. Addit. Manuf. 36, 101726 (2020).

[8] Shi R, Khairallah SA, Roehling TT, Heo TW, McKeown JT, Matthews MJ. Microstructural control in metal laser powder bed fusion additive manufacturing using laser beam shaping strategy. Acta Mater. 184, 284–305 (2020).

[9] Maina MR, Okamoto Y, Okada A, Närhi M, Kangastupa J, Vihinen J. High surface quality welding of aluminum using adjustable ring-mode fiber laser. J. Mater. Process. Technol. 258, 180–188 (2018).

[10] Sun T, Ferguson N, Liu C, Gibbons G, Franciosa P. Application of adjustable ring mode laser in remote laser welding of additive manufactured AlSi10Mg alloy. J. Laser Appl. 34(4), 042007 (2022).

[11] Galbusera F, Caprio L, Previtali B, Demir AG. The influence of novel beam shapes on melt pool shape and mechanical properties of LPBF produced Al-alloy. J. Manuf. Process. 85, 1024–1036 (2023).

[12] Nahr F, Bartels D, Rothfelder R, Schmidt M. Influence of Novel Beam Shapes on Laser-Based Processing of High-Strength Aluminium Alloys on the Basis of EN AW-5083 Single Weld Tracks. J. Manuf. Mater. Process. 7(3), 93 (2023).
[13] Shao G, Tsakiropoulos P, Miodownik AP. Role of nucleation in phase competition in binary Ti-Al alloys. Mater. Sci. Technol. 13(10), 797–805 (1997).
[14] Opprecht M, Garandet J-P, Roux G, Flament C. An understanding of duplex microstructures encountered during high strength aluminium alloy laser beam melting processing. Acta Mater. 215, 117024 (2021).
[15] Cahill JA, Grosse AV. Viscosity and Self-Diffusion of Liquid Thallium from Its Melting Point to About 1300°K. J. Phys. Chem. 69(2), 518–521 (1965).
[16] Vázquez J, López-Alemany PL, Villares P, Jiménez-Garay R. Generalization of the Avrami equation for the analysis of non-isothermal transformation kinetics. Application to the crystallization of the Cu 0.20 As 0.30 Se 0.50 alloy. J. Phys. Chem. Solids 61(4), 493–500 (2000).
[17] Mohebbi MS, Ploshikhin V. Simulation of Primary Particle Development and Their Impact on Microstructural Evolution of Sc-Modified Aluminum Alloys during Additive Manufacturing. Metals 11(7) (2021).
[18] Romanova V, Mohebbi MS, Dymnich E, Balokhonov R, Ploshikhin V. A physically-based computational approach for processing-microstructure-property linkage of materials additively manufactured by laser powder bed fusion. Int. J. Mech. Sci. 219, 107103 (2022).
[19] Zhao C, Shi B, Chen S et al. Laser melting modes in metal powder bed fusion additive manufacturing. Rev. Mod. Phys. 94(4), 045002 (2022).
[20] Li JH, Oberdorfer B, Wurster S, Schumacher P. Impurity effects on the nucleation and growth of primary Al3(Sc,Zr) phase in Al alloys. J. Mater. Sci. 49(17), 5961–5977 (2014).